(Received 23 September 2024, Accepted 22 October 2024, Scheduled 30 October 2024)

Digital Non-Foster Impedance Design for Wideband Electrically Small Antennas Beyond the Chu Limit

Christopher Daniel Jr.[1] and Thomas Weldon[2,*]

[1] *Department of Physics, University of New Mexico, Albuquerque, NM 87131, USA*
[2] *Waxhaw, NC 28173, USA*

ABSTRACT: Although initial results for the digital implementation of non-Foster impedances showed promise for increasing the bandwidth of electrically small antennas beyond the Chu limit, earlier approximate design methods were inadequate to fully describe the complexity of digital impedance circuits. Recently, the input impedance of such digital impedance circuits was discovered to be dependent on the external source impedance of the driving source. Furthermore, this dependence on the driving source impedance was shown to be extraordinarily complicated, even for a purely resistive driving source. Consequently, the digital non-Foster impedance match of an antenna is considerably more complicated, even with a lumped-element antenna model. In this paper, we present a method for designing a stable wideband digital non-Foster circuit to match the impedance of an electrically small dipole antenna. Simulation results confirm the theoretical predictions and efficacy of the design method in producing VSWR bandwidth beyond the Wheeler-Chu limit. An RLC model of a 10 MHz electrically small dipole with Q of 215 and passive-tuned bandwidth of 46.5 kHz is chosen to demonstrate the proposed method. For this antenna with Wheeler-Chu bandwidth limit of 442 kHz and size parameter ka = 0.42 rad, the proposed method results in achieving an impedance bandwidth of 2.3 MHz, or more than five times the Wheeler-Chu limit and 48 times the passive-tuned bandwidth. Lastly, the mid-band noise figure is 12.7 dB when the proposed design is combined with a receiver having 3 dB noise figure.

1. INTRODUCTION

The design of an electrically small antenna (ESA) with bandwidth greater than the Wheeler-Chu limit remains an area of active research [1, 2]. In a wide-ranging survey, the Wheeler-Chu bandwidth limit was confirmed for over 100 passive ESA designs [3]. In a more recent survey of ESAs at low frequency, active non-Foster ESA designs were noted to provide bandwidth greater than the Wheeler-Chu limit, while passive ESA designs were constrained by the Wheeler-Chu limit [4]. These earlier wideband ESA designs used non-Foster devices such as negative capacitors or negative inductors, implemented by a variety of analog circuits including negative impedance converters and current conveyors [5–10]. Examples of analog non-Foster ESA designs with bandwidth greater than the Wheeler-Chu limit include a 403–419 MHz near-field resonant parasitic ESA [11], a 26–89 MHz monopole transmitting ESA [12], a 40 MHz resonant antenna with tripled bandwidth [13], a 30–135 MHz high-power ESA [14], a 29–39 MHz self-oscillating ESA [15], a 30–200 MHz monopole ESA [16], a resonant printed monopole ESA with quintupled bandwidth [17], and an acoustic piezoelectric transducer [18]. Other alternatives, such as time-varying systems, are also making inroads to increasing bandwidth [19–21]. A receiver bandwidth of 10 MHz was obtained for a 93 mm loop antenna at 100 MHz by using Bode-Fano mismatch combined with a low-noise pumped-varactor parametric amplifier [21–24]. Notwithstanding such successful efforts to exceed the Wheeler-Chu bandwidth limit by utilizing analog non-Foster circuits, design challenges remain in areas such as maintaining stability with system variations due to component tolerances and due to antenna impedance variations when objects come into close proximity of the antenna [4, 25–29].

Digital non-Foster impedance circuits provide an alternative approach to analog circuit implementations of non-Foster devices such as negative capacitors and negative inductors [30–33]. One potential advantage of digital non-Foster circuits is that the Nyquist limit constrains the frequency range of potential digital feedback instability oscillation to half the sampling frequency, whereas analog designs can become unstable and oscillate at frequencies much higher than the operating band. Other potential advantages include the reduction in component variation by using digital circuits, along with the potential for digital implementation of adaptive stabilization of antenna impedance variations due to nearby objects. In addition, the topology of digital non-Foster circuits for ESA enhancement is similar to modern radio architectures, potentially enabling low-frequency wireless internet of things devices to take advantage of the 7.8 dB reduction in the urban Friis-equation propagation loss each time the frequency is halved [4, 34–36].

Despite early successes [33, 37], prior approximate methods for designing digital non-Foster circuits seem ineffective in matching high-Q ESA impedances and in using 50-ohm high-speed analog-to-digital converters (ADC) and digital-to-analog converters (DAC). Recently, we discovered that the impedance of a digital non-Foster circuit is dependent on the impedance of the external source that is driving the digital non-Foster cir-

* Corresponding author: Thomas Weldon (tpw@ieee.org).

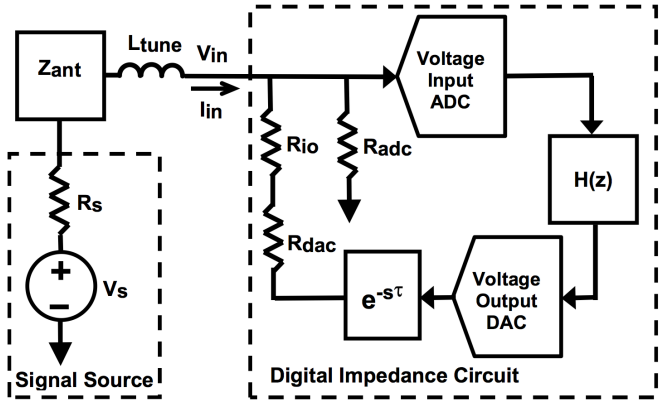

FIGURE 1. Block diagram of a digital impedance circuit driven by an external voltage source $V_s(s)$ with external source resistance R_s in series with an antenna defined by its impedance Z_{ant} and an optional tuning inductor L_{tune}. The digital filter $H(z)$ sets the impedance at node V_{in} to $Z_{in}(s) = V_{in}(s)/I_{in}(s)$, and time delay τ accounts for computational latency. Resistor R_{io} couples the DAC output impedance R_{dac} to the ADC input impedance R_{adc}.

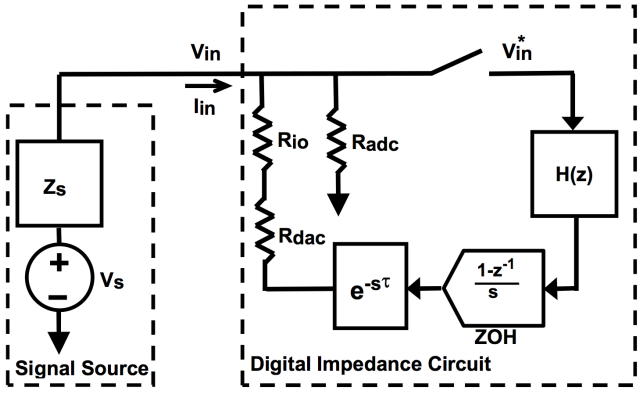

FIGURE 2. Analysis block diagram of the system in Fig. 1, showing the effective source impedance $Z_s(s) = R_s + Z_{ant}(s) + sL_{tune}$ driving the digital impedance circuit. The ADC is modeled as a sampler whose output $V^\star_{in}(s)$ is the starred transform of $V_{in}(s)$, and the DAC output is modeled as the output of the ZOH $(1 - z^{-1})/s$, with time delay τ representing computational latency.

cuit [30, 38]. Even in the simple case of a purely resistive source, this unexpected dependence on the source impedance results in a complicated expression for the digital non-Foster circuit impedance [30, 38]. Consequently, this dependence on the driving source impedance leads to a more complicated digital impedance design procedure for antennas. Therefore, in this paper we consider the challenging problem of designing a stable digital non-Foster circuit for greatly increasing ESA impedance bandwidth. Our proposed method for designing stable digital non-Foster ESA matching networks with bandwidth in excess of the Wheeler-Chu limit builds upon our recent design procedure for digital impedance circuits with resistive sources [30].

In the next section, we develop the theory for determining digital circuit impedance when the driving source impedance is a lumped-element model of an ESA. Using this theoretical foundation, we present a design method for determining digital filter parameters to achieve an overall stable system that enables ESA bandwidth beyond the Wheeler-Chu limit. Lastly, we present simulation results for stable digital non-Foster ESA designs using our design method that have bandwidths surpassing the Wheeler-Chu limit.

2. THEORETICAL ANALYSIS

To begin, consider the digital impedance circuit of Fig. 1 that is analyzed by using the block diagram of Fig. 2. In transmitter mode, the voltage source $V_s(s)$ with source resistance R_s in the dashed box of Fig. 1 drives the antenna impedance $Z_{ant}(s)$ in series with an optional tuning inductor L_{tune}. In receiver mode, the antenna acts as the signal source, and R_s would represent the receiver input impedance. For the analysis, the source and antenna impedance are combined and treated as an effective source impedance $Z_s(s) = R_s + Z_{ant}(s) + sL_{tune}$ in the dashed box on the left side of Fig. 2. The digital impedance circuit with input voltage $V_{in}(s)$ and input current $I_{in}(s)$ is shown in the dashed box on the right of both figures. In Fig. 2, $V^\star_{in}(s)$ is the starred transform[1] of $V_{in}(s)$ [39]. The ADC of Fig. 1 is modeled by the ideal sampler with sampling period T in Fig. 2, with the sampler output $V^\star_{in}(s)$ being the input to the digital filter $H(z)$. The DAC output is modeled by passing the digital filter output through the zero-order hold (ZOH) with transfer function $(1-z^{-1})/s$. The ZOH output in Fig. 2 passes through time delay $e^{-s\tau}$ which models any latency due to digital filter computation. The ADC input impedance is R_{adc}; the DAC output impedance is R_{dac}; and R_{io} couples the DAC output to the ADC input.

The input voltage $V_{in}(s)$ is given by [38]:

$$V_{in}(s) = \left. \frac{\frac{V_s(s)}{Z_s(s)} + \frac{V^\star_{in}(s)e^{-s\tau}H(z)(1-z^{-1})/s}{R_{io}+R_{dac}}}{\frac{Z_s(s)+R_e}{Z_s(s)R_e}} \right|_{z=e^{sT}}, \quad (1)$$

where T is the sampling period of the ADC and DAC, and $R_e = R_{adc}(R_{dac}+R_{io})/(R_{adc}+R_{dac}+R_{io})$ is the resistance of the parallel combination of R_{adc} with $R_{dac} + R_{io}$. Applying the starred transform [39] to both sides of (1) gives

$$V^\star_{in}(s) = \left(\frac{R_e V_s(s)}{R_e + Z_s(s)}\right)^\star + \left. \frac{R_e V^\star_{in}(s) H(z)(1-z^{-1})K(z)}{R_{io}+R_{dac}} \right|_{z=e^{sT}}, \quad (2)$$

where $K(z)$ is defined as the modified z-transform[2] [39] of $K(s) = Z_s(s)e^{-s\tau}s^{-1}(R_e + Z_s(s))^{-1}$.

To prevent aliasing, the input $V_s(s)$ is bandlimited, ensuring that input $V_s(s) = 0$ for continuous-time angular frequencies $\omega > \pi/T$. Therefore, $(R_e V_s(s)) / (R_e + Z_s(s)) = 0$

[1] The starred transform is used in digital control theory to analyze systems that include a mixture of analog circuits and digital circuits. In the time domain, the starred transform $v^\star(t)$ of a continuous-time signal $v(t)$ is equivalent to multiplying the signal by a periodic Dirac impulse train. In the Laplace domain, the starred transform is the Laplace transform of $v^\star(t)$.

[2] In the analysis of a sampled signal, the modified z-transform is a type of z-transform that properly accounts for continuous-time delays in a sampled signal that may be a fraction of a clock period.

and $R_e + Z_s(s) \neq 0$ for $\omega > \pi/T$ and passive $Z_s(s)$ with $R_e > 0$. Thus, the entire term $(R_e V_s(s))/(R_e + Z_s(s))$ is also bandlimited, having a value of zero for $\omega > \pi/T$. Lastly, we note that the starred transform of a bandlimited function, such as $F(s)$, without aliasing equals $F(s)/T$ for frequencies below half the sampling rate[3]. Thus, (2) becomes

$$V_{in}^{\star}(s) \approx \frac{V_s(s)L(s)}{T} + \frac{R_e V_{in}^{\star}(s) H(z)(1-z^{-1})K(z)}{R_{io}+R_{dac}}\bigg|_{\substack{z=e^{sT} \\ \omega<\pi/T}} \quad (3)$$

for frequencies $\omega < \pi/T$, where $L(s) = R_e/(R_e + Z_s(s))$.

While (3) may be the most accurate equation for finding a filter $H(z)$ to achieve a desired digital impedance, an approximation of (3) is used for determining the stability in the z-plane[4]. To find this z-domain approximation for $\omega < \pi/T$, we first define the bilinear transform[5] [40] of $L(s)$ as

$$L(z) = \frac{R_e}{R_e + Z_s(s)}\bigg|_{s=\frac{2}{T}\frac{z-1}{z+1}}, \quad (4)$$

noting that a pre-warped bilinear transform can optionally be used. To determine stability in the z-plane, (3) can then be approximated by

$$V_{in}^{\star}(s) \approx \frac{V_s(s)L(z)}{T} + \frac{R_e V_{in}^{\star}(s) H(z)(1-z^{-1})K(z)}{R_{io}+R_{dac}}\bigg|_{\substack{z=e^{sT} \\ \omega<\pi/T}}. \quad (5)$$

Comparing Fig. 1 and Fig. 2, the effective overall source impedance $Z_s(s)$ in Fig. 2 is source resistance R_s in series with the antenna impedance $Z_{ant}(s)$ and the optional tuning inductor L_{tune}:

$$Z_s(s) = R_s + Z_{ant}(s) + sL_{tune}, \quad (6)$$

where the antenna impedance is

$$Z_{ant}(s) = \frac{1}{sC_{31}} + \frac{R_{31}L_{31}s}{R_{31}L_{31}C_{32}s^2 + L_{31}s + R_{31}}, \quad (7)$$

with C_{31}, L_{31}, R_{31}, and C_{32} as specified by the ESA dipole antenna impedance model in [41]. While more complicated dipole impedance models exist, the model in (7) suffices for designing electrically small dipole antennas, particularly where higher order resonances of the antenna exceed the Nyquist limit frequency of $0.5/T$. Note that the proposed methods are applicable to antenna models having the general form of the second-order polynomial in (7), and the overall framework of our methods should be adaptable for other polynomial ESA models.

For the dipole antenna model in (7), the modified z-transform $K(z)$ in (3) and (5) is obtained from the partial fraction expansion of $K(s)$:

$$K(s) = \frac{Z_s(s)e^{-s\tau}}{s(R_e + Z_s(s))} = e^{-s\tau}\left(\frac{d_0}{s-s_0} + \sum_{n=1}^{n_{\max}} \frac{d_n}{s-s_n}\right), \quad (8)$$

where the $n_{\max}+1$ poles of $K(s)$ at s_n include a fixed pole at $s_0 = 0$. The value of $n_{\max}$ is $n_{\max} = 4$ when a tuning inductor $L_{tune} \neq 0$ is employed, and $n_{\max} = 3$ when $L_{tune} = 0$. Then, the corresponding modified z-transform becomes

$$K(z) = z^{-\lambda}\left(\frac{d_0}{z-1} + \sum_{n=1}^{n_{\max}} \frac{d_n e^{s_n m T}}{z - e^{s_n T}}\right), \quad (9)$$

where m and λ are given as

$$m = 1 - \tau/T + \lambda \text{ for } \lambda = floor(\tfrac{\tau}{T}) \quad (10)$$

where $floor(y)$ is the integer less than or equal to y. The input current of the digital impedance circuit of Fig. 2 is found by the voltage difference between the source and the input divided by the source impedance:

$$I_{in}(s) = \frac{V_s(s) - V_{in}(s)}{Z_s(s)}. \quad (11)$$

Using a commercial symbolic solver, we find that the input impedance of the digital impedance circuit is:

$$Z_{in}(s) = \frac{V_{in}(s)}{I_{in}(s)} = \frac{A(s,z)H(z) + B(s,z)}{C(s,z)H(z) + D(s,z)}\bigg|_{z=e^{sT}}, \quad (12)$$

where

$$\begin{aligned} A(s,z) =& \left(R_{adc}\left(R_{dac}+R_{io}\right)(1-z)\right. \\ & \left.(R_e K(z) sT e^{s\tau} - L(s)Z_s(s))\right)|_{z=e^{sT}} \end{aligned} \quad (13)$$

$$B(s,z) = R_{adc}\left(R_{dac}+R_{io}\right)^2 zsTe^{s\tau}\Big|_{z=e^{sT}}$$

$$\begin{aligned} C(s,z) =& \left(R_e\left(R_{adc}+R_{dac}+R_{io}\right)(1-z)\,K(z)sTe^{s\tau}\right. \\ & \left.+R_{adc}(R_{dac}+R_{io})\left(1-z\right)L(s)\right)|_{z=e^{sT}} \\ D(s,z) =& \left(R_{adc}+R_{dac}+R_{io}\right)\left(R_{dac}+R_{io}\right) zsTe^{s\tau}|_{z=e^{sT}}. \end{aligned}$$

3. DESIGN PROCEDURE

The overall goal is to design a digital filter $H(z)$ in Fig. 1 that produces a desired digital non-Foster circuit impedance $Z_{in}(s) = V_{in}(s)/I_{in}(s)$, providing a stable non-Foster impedance match to an ESA with a voltage standing wave ratio (VSWR) bandwidth greater than the Wheeler-Chu limit. In our experiments with wideband ESA matching, we have found that a third-order $H(z)$ usually suffices:

$$H(z) = \frac{b_0 z^3 + b_1 z^2 + b_2 z + b_3}{z^3 + a_1 z^2 + a_2 z + a_3}, \quad (14)$$

with seven digital filter parameters $b_0, b_1, b_2, b_3, a_1, a_2, a_3$ to be determined.

The important question we now address is how to efficiently search the 7-dimensional parameter space for the parameters $b_0, b_1, b_2, b_3, a_1, a_2, a_3$ which produce a stable solution, if one exists. To begin, we derive a system of six linear equations by choosing three frequencies s_1, s_2, and s_3, and setting the desired goals for the digital impedance to be $Z_{in}(s_1)$, $Z_{in}(s_2)$,

[3] The starred transform $F^{\star}(s)$ can be considered as a periodic extension of Laplace transform $F(s)$ that repeats at multiples of the sampling frequency with magnitude scaled by a factor of $1/T$.

[4] In the z-domain, a system is stable when all poles lie within the unit circle of the z-plane, $|z| < 1$.

[5] The bilinear transform can be used to convert a stable Laplace-domain system $H(s)$ into a corresponding stable discrete-time system $H(z)$.

and $Z_{in}(s_3)$ at those frequencies. For an ESA, the three frequencies chosen to control the digital impedance are typically the center frequency along with the two edge frequencies of the operating frequency band. By substituting (14) into (12), and then rearranging the real and imaginary terms, we get:

$$\begin{aligned}
&Re((C(s_i,z)Z_{in}(s_i)-A(s_i,z))z^3)b_0 \\
&\quad + Re((C(s_i,z)Z_{in}(s_i)-A(s_i,z))z^2)b_1 \\
&\quad + Re((C(s_i,z)Z_{in}(s_i)-A(s_i,z))z)b_2 \\
&\quad + Re(C(s_i,z)Z_{in}(s_i)-A(s_i,z))b_3 \\
&\quad - Re((B(s_i,z)-D(s_i,z)Z_{in}(s_i))z^2)a_1 \\
&\quad - Re((B(s_i,z)-D(s_i,z)Z_{in}(s_i))z)a_2 \\
&\quad - Re(B(s_i,z)-D(s_i,z)Z_{in}(s_i))a_3 \\
&= Re((B(s_i,z)-D(s_i,z)Z_{in}(s_i))z^3)\big|_{z=e^{s_iT}} \\
&Im((C(s_i,z)Z_{in}(s_i)-A(s_i,z))z^3)b_0 \\
&\quad + Im((C(s_i,z)Z_{in}(s_i)-A(s_i,z))z^2)b_1 \\
&\quad + Im((C(s_i,z)Z_{in}(s_i)-A(s_i,z))z)b_2 \\
&\quad + Im(C(s_i,z)Z_{in}(s_i)-A(s_i,z))b_3 \\
&\quad - Im((B(s_i,z)-D(s_i,z)Z_{in}(s_i))z^2)a_1 \\
&\quad - Im((B(s_i,z)-D(s_i,z)Z_{in}(s_i))z)a_2 \\
&\quad - Im(B(s_i,z)-D(s_i,z)Z_{in}(s_i))a_3 \\
&= Im((B(s_i,z)-D(s_i,z)Z_{in}(s_i))z^3)\big|_{z=e^{s_iT}}, \qquad (15)
\end{aligned}$$

for the index $i = 1, 2, 3$, corresponding to each of the three chosen design frequencies s_1, s_2, and s_3. This results in an underdetermined system of six linear equations with seven unknown variables b_0, b_1, b_2, b_3, a_1, a_2, and a_3. Note that if we chose a form of $H(z)$ with only six parameters, this would yield a unique solution to (15), but with no guarantee of stability. This underdetermined system of linear equations gives us added flexibility to find a stable solution if one exists.

The flexibility of having an extra degree of freedom from the seventh parameter allows us to search for a stable solution, as in [30]. We choose a_1 as the free variable to search for digital filter coefficients that result in a stable system. The motivation for choosing a_1 as our free variable is discussed later, after we first consider the system stability analysis below.

To determine overall stability, the z-domain transfer function $G(z)$ of the system is derived from (5), which becomes

$$V_{in}(z) \approx V_s(z)L(z) + \frac{R_e V_{in}(z)H(z)(1-z^{-1})K(z)}{R_{io}+R_{dac}}\bigg|_{\substack{z=e^{sT}\\ \omega<\pi/T}}, \qquad (16)$$

upon substituting $V_{in}^{\star}(s) = V_{in}(z)|_{z=e^{sT}}$ and $V_s(s)/T = V_s(z)|_{z=e^{sT}}$. Rearranging (16) yields the transfer function $G(z)$, which determines the overall system poles for stability[6]:

$$G(z) = \frac{V_{in}(z)}{V_s(z)} \approx \frac{L(z)}{1 - R_e H(z)(1-z^{-1})K(z)/(R_{io}+R_{dac})}. \qquad (17)$$

[6] In digital control theory, stability analysis of a system composed of a mixture of analog and digital circuits is commonly conducted in the z-domain, where stability is assured when all poles lie within the unit circle of the z-plane.

In (17), observe that the poles of the system include the zeroes of the denominator of (17) along with the poles of $L(z)$. The stability of $L(z)$ is evident, since the bilinear transform maps the stable poles of $L(s)$ to stable poles in $L(z)$. Given $R_e > 0$, and a passive antenna RLC model $Z_s(s) = R_s + Z_{ant}(s) + sL_{tune}$ in (6), and with (7) being a positive real function[7], it follows that $L(s)$ is also a positive real function [42]. With $Re(R_e + Z_s(j\omega)) > 0$ assuring that $L(s)$ can have no poles on the $j\omega$ axis[8], then the poles of $L(s)$ are always in the open left half s-plane, and are therefore always stable.

The remaining system poles are the zeroes of the denominator in (17), so the system is stable if and only if those zeroes are inside the unit circle of the z-plane [39]. Rearranging the denominator of (17), we get

$$z = \rho\, H(z)\,(z-1)\,K(z), \qquad (18)$$

where $\rho = R_e/(R_{io}+R_{dac})$. The roots of (18) are dependent on our controllable filter $H(z)$, which includes our tunable free variable a_1 that adjusts the system's overall stability. Care must also be taken with the cancellation of the $z-1$ term in (18) and the $z-1$ term in the denominator of at least one of the terms contained in $K(z)$ in (9).

For practical implementation, the following analysis only considers delay times between one and two clock cycles, $T < \tau < 2T$. This affects the modified z-transform of $K(z)$ in (18) resulting in $\lambda = 1$ in (10) and a leading factor of z^{-1} in (9). Substituting $H(z)$ from (14) into (18) with $L_{tune} > 0$ and $n_{\max} = 4$ yields the following general constraint equation for a stable system:

$$z^9 + c_8 z^8 + \sum_{n=0}^{7} c_n z^n = \prod_{n=1}^{9}(z - z_{pn}) = 0 \qquad (19)$$

for time delay $T < \tau < 2T$, where z_{pn} is the n^{th} pole in the denominator of (17), and $c_8 = a_1 - \sum_{n=1}^{n_{\max}} e^{s_n T}$. From (18) and (19) it follows that

$$\begin{aligned}
|c_8| &= \left| a_1 - \sum_{n=1}^{n_{\max}} e^{s_n T} \right| = \left| -\sum_{n=1}^{9} z_{pn} \right| < 9 \\
\implies \quad |a_1| &< 9 + \left| \sum_{n=1}^{n_{\max}} e^{s_n T} \right| < 13 \qquad (20)
\end{aligned}$$

where $|z_{pn}| < 1$ for a stable system, and the real part $Re\{s_n\} \leq 0$ since $K(s)$ is a positive real function as noted later below. The first inequality in (20) serves as an upper bound for $|c_8|$, and the second inequality serves as an upper bound for $|a_1|$.

[7] Passive RLC circuits with positive-valued elements have positive real impedance functions. The poles and zeroes of a positive real function $Z(s)$ are all in the closed left-half Laplace plane, and the real part of a positive real function $Z(s)$ is greater than or equal to zero when the real part of s is greater than equal to zero.

[8] The real part of $R_e + Z_s(j\omega)$ cannot equal zero on the $s = j\omega$ axis for $R_e > 0$, since positive real $Z_s(s)$ assures that $Re(Z_s(j\omega)) \geq 0$. So, it follows that $R_e + Z_s(j\omega)$ cannot equal zero on the $s = j\omega$ axis since its real part cannot equal zero.

The constant c_8 is of particular importance since it constrains the search for stable solutions to a limited range of possible a_1 values.

For all poles to be stable, we must have $|z_{pn}| < 1$ for all n, and so $|\sum_{n=1}^{9} z_{pn}| \leq \sum_{n=1}^{9} |z_{pn}| < 9$. Furthermore, with $Z_s(s) = R_s + Z_{ant}(s) + sL_{tune}$ in (6) and (7) being a positive real function, then $K(s)$ is also a positive real function. This means that every s_n must be a pole in the closed left half s-plane, and therefore the real part of every s_n must be less than or equal to zero. This condition thus constrains $|a_1|$ to be no larger than $5 + 2\,n_{\max}$ for a general $n_{\max}$ and any choice of positive circuit parameters in Fig. 1. Choosing a_1 to be the free variable has been observed to yield a smaller search range than other parameters in $H(z)$.

Therefore, the free variable a_1 from (14) must be a real number between $-5 - 2n_{\max} < a_1 < 5 + 2n_{\max}$, if a stable solution exists. Although a stable system guarantees that $|a_1| < 5 + 2n_{\max}$, the converse is not true, and a stable system may not exist. Nonetheless, this result greatly reduces our search space by eliminating the need to search a_1 values outside the foregoing range. Note that for each value of a_1 in the search, the remaining six coefficients needed to determine $H(z)$ in (14) will be given by the straightforward solution of the six linear equations in (15). If no stable solution is found in the search, either the number of a_1 values within the range $|a_1| < 5+2n_{\max}$ needs to be increased when searching, or a stable solution does not exist for the system altogether.

In the search process, stability of each $H(z)$ solution is verified by determining the roots of (19). According to Abel's impossibility theorem, the nine roots in (19) cannot be found in closed form for the coefficients $c_0 - c_8$. Therefore, an efficient numerical root finding algorithm is necessary to solve for the roots in (19) to determine if a stable solution exists for each a_1 value in the search. The computational complexity of the search space for our proposed design method is $O(n)$ where n is the number of a_1 values to search over. The proposed design method greatly reduces the search space compared to a brute force search method with a computational complexity of $O(n^7)$ when considering n search values over each dimension of the seven $H(z)$ parameters $b_0, b_1, b_2, b_3, a_1, a_2, a_3$. Similar to the search in [30], our free variable in the proposed design method will also have a significantly reduced search space with $|a_1| < 5 + 2n_{\max}$ rather than $|a_1| < \infty$.

Lastly, the target application of the design method is to implement a digital non-Foster impedance match with an ESA that exceeds the Wheeler-Chu bandwidth-efficiency limit [3]:

$$B\eta = \frac{1}{\sqrt{2}/(ka) + \sqrt{2}/(ka)^3} \tag{21}$$

for a linear polarization dipole antenna, where impedance bandwidth is at VSWR = 2; B is the fractional bandwidth; η is the antenna efficiency; a is the radius of a sphere that would enclose the antenna; $k = \omega_o/c$; and ω_o is the operating center frequency in rad/s. Therefore, it is desirable to choose the edge frequencies s_1 and s_3 in (15) to be beyond the Wheeler-Chu limit, if possible. It is also natural to choose s_2 in (15) to be the center frequency for better control of the impedance between the two edge frequencies.

In summary, our proposed design method for wideband digital non-Foster impedance matching of an ESA is to:

- search a_1 values over the range $|a_1| < 5 + 2n_{\max}$, or $-9 - \left|\sum_{n=1}^{n_{\max}} e^{s_n T}\right| < a_1 < 9 + \left|\sum_{n=1}^{n_{\max}} e^{s_n T}\right|$,
- for each a_1 value in the search, solve for the remaining parameters b_0, b_1, b_2, b_3, a_2, a_3 in $H(z)$ by using the six linear equations in (15),
- for each $H(z)$, determine the overall system stability from the pole locations z_{pn} in (19),
- choose the most stable solution found in the search, such that $\max(|z_{pn}|)$ is minimized.

In the next section, two examples illustrate the foregoing digital non-Foster impedance design method for an electrically small dipole antenna, yielding impedance bandwidths greater than the Wheeler-Chu limit.

4. DESIGN EXAMPLES

Two example designs are used to demonstrate the efficacy of the proposed design method to significantly increase the bandwidth of electrically small dipole antennas. In the examples, the dipole antenna has a total length of $L = 4\,\text{m}$, with each dipole arm of length $h_a = L/2 = 2\,\text{m}$ and arm radius $r_a = h_a/50 = 0.04\,\text{m}$, and has a nominal fundamental resonant frequency of approximately 35 MHz. This dipole is modeled as an ESA by using (7) with the following parameters: $R_{31} = 1013\,\Omega$, $L_{31} = 953.1\,\text{nH}$, $C_{31} = 18.92\,\text{pF}$, and $C_{32} = 3.943\,\text{pF}$. At 10 MHz, the dipole impedance is $Z_{ant}(s) = 3.635 - j780.6$, with $Q = 215$. In each example, the design impedance goals are heuristic as a demonstration for proof of concept. Since these heuristic impedance goals are not optimal, future incorporation of optimization techniques may yield improved results.

The first design example in the schematic of Fig. 3 was simulated in the Simulink commercial simulator, where source resistance $Rs1$ corresponds to R_s in Fig. 1 and equals the antenna radiation resistance at the chosen design operating center frequency $f_2 = s_2/(j2\pi) = 10\,\text{MHz}$ as shown in Table 1. This example also includes an added passive-tuning inductor $L_{tune} = 12.42\,\mu\text{H}$ in Fig. 3 that cancels the capacitive reactance of the antenna at the center frequency f_2. The digital non-Foster impedance circuit in Fig. 3 is composed of the "Zero-Order Hold" block that implements a sampler with sampling period T and drives digital filter $H(z)$, followed by time delay τ to account for the computational latency. Resistor R_{adc} is the ADC input resistance; R_{dac} is the DAC output resistance; and R_{io} couples the DAC output to the ADC input. The ideal voltage source measurement in Fig. 3 is shown as "Vs," and the current measurement at the source is shown as "Iin." In the time domain simulations of the examples that follow, the source excitation was a narrow pulse, and the circuit responses were observed to decay in a stable manner, confirming stability of the designs. Thus, the impedance seen by the voltage

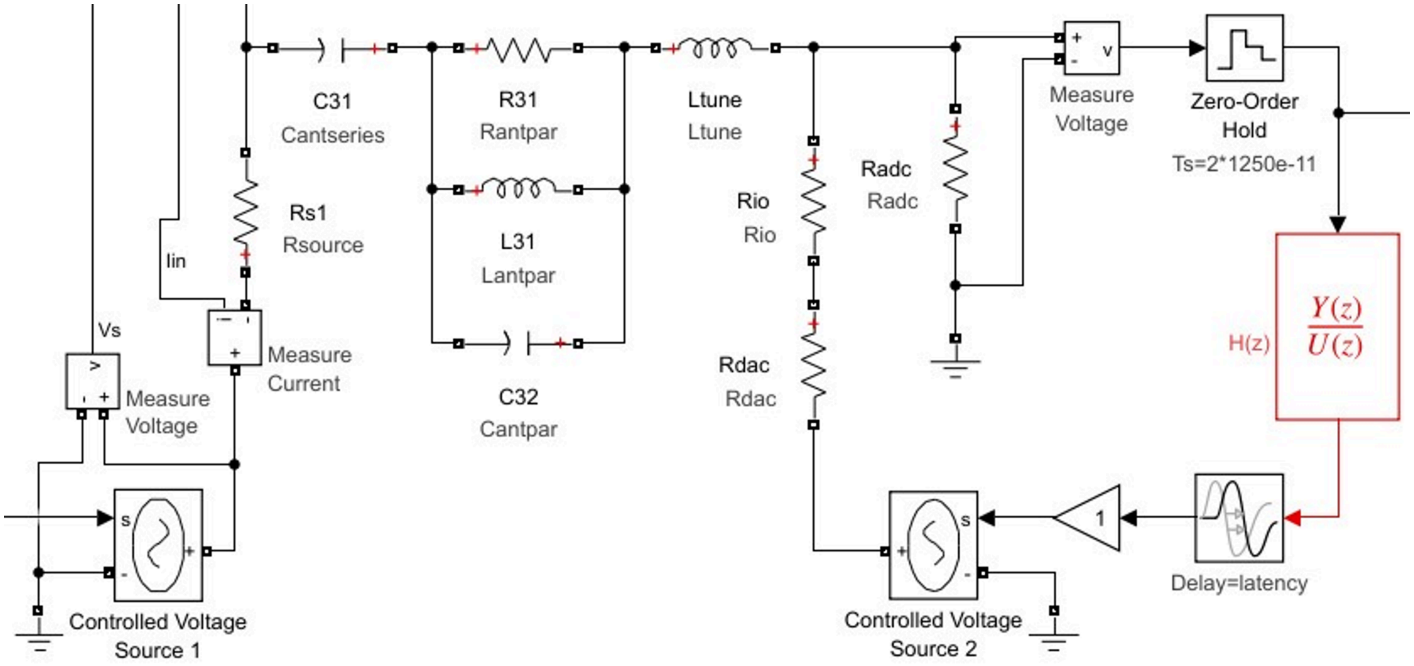

FIGURE 3. Simulink schematic excerpt of the first example, where source resistance $Rs1 = 3.635$ equals the antenna radiation resistance at center frequency $f_2 = 10\,\text{MHz}$ given in Table 1. The antenna model is comprised of $C_{31} = 18.92\,\text{pF}$, $L_{31} = 953.1\,\text{nH}$, $R_{31} = 1013\ \Omega$, and $C_{32} = 3.943\,\text{pF}$. The digital impedance circuit has a $T = 25\,\text{ns}$ sampler in the "Zero-Order Hold" block. The sampler is followed by digital filter $H(z)$ given in Table 1, and a latency time delay of $3T/2 = 37.5\,\text{ns}$ is included. The ADC input and DAC output impedances are $R_{adc} = R_{dac} = 30\,\text{k}\Omega$, and are coupled through feedback resistor $R_{io} = 30\,\text{k}\Omega$. Antenna tuning inductor $L_{tune} = 12.42\,\mu\text{H}$ cancels the capacitive antenna reactance at center frequency f_2.

source "Controlled Voltage Source 1" is computed in the simulation as the ratio of the fast Fourier transforms (FFTs) of the two time-domain measurements, "FFT(Vs)/FFT(Iin)." Further details can be found in the dataset for all examples in [43], with encryption password aa4488gg.

The digital filter $H(z)$ in Table 1 and Fig. 3 is computed using the proposed design method, given the design goals in Table 1 for the non-Foster impedance $Z_{in}(s_1)$, $Z_{in}(s_2)$, and $Z_{in}(s_3)$ at the three design frequencies f_1, f_2, and f_3. As can be seen in Table 1, the goals for $Z_{in}(s)$ approximately cancel the reactance of the passively-tuned antenna *including* L_{tune}, with a residual small resistance and a residual small reactance with positive slope. In addition, the corresponding design goal and simulation result for the total impedance $Z_{tot}(s) = Z_{in}(s) + Z_{ant}(s) + sL_{tune}$ are also given in Table 1 at the three design frequencies. The digital filter design $H(z)$ achieves the specified impedance targets $Z_{tot}(s)$ at the three design frequencies, effectively neutralizing most of the antenna reactance. Simulation results in Table 1 confirm the design's effectiveness, achieving near-target design goals at the specified frequencies.

In the top plot of Fig. 4 for this first example, simulation results for $Z_{tot}(s) = Z_{ant}(s) + sL_{tune}(s) + Z_{in}(s)$ are plotted as the solid curves, along with $\times$'s showing the theoretical $Z_{tot}(s)$. The solid red curve shows the real part $Re[Z_{tot}(s)]$, and the solid blue curve shows the imaginary part $Im[Z_{tot}(s)]$. The real and imaginary parts of a passively-tuned antenna using L_{tune} are shown in the dashed magenta and dashed cyan curves, respectively. Both the real and imaginary parts of the simulated $Z_{tot}(s)$ closely match the theoretical $Z_{tot}(s)$ in the top plot of Fig. 4.

As shown in the middle plot of Fig. 4, the VSWR = 2 bandwidth of the simulation was 2.30 MHz centered around 9.9 MHz. The Wheeler-Chu bandwidth-efficiency product from (21) is $B\eta = 0.0442$, or approximately 440 kHz at a center frequency of 10 MHz with $ka = 0.42$ rad. This first example demonstrates the design's effectiveness in increasing the bandwidth to approximately $2.3/0.442 = 5.2$ times the Wheeler-Chu limit for $\eta = 1$ (or 4.15 if we let $\eta \approx 3.63/4.57 = 0.795$ attributable to the added $0.93\,\Omega$ in $Z_{in}(s_2)$ at f_2 as indicated in Table 1). The 2.3 MHz bandwidth is 48.9 times the theoretical passive-tuned antenna bandwidth of approximately 10/Q = 10/215 MHz or 47 kHz in the dashed cyan curve, which is too narrow to be observed in the middle plot.

The bottom plot of Fig. 4 displays the simulated noise figure as a solid blue curve, along with $\times$'s showing the theoretical noise figure. The dashed cyan curve shows theoretical noise figure of a passively-tuned antenna using L_{tune}. The noise figure is also noted in Table 1 at design frequencies f_1, f_2, and f_3. The noise figure NF is calculated from the simulation as:

$$NF = 10\ \log_{10}\left(\frac{e_{ant}^2 + \sum e_n^2}{e_{ant}^2}\right), \tag{22}$$

where $\sum e_n^2$ represents the total sum of squared noise voltages referred back to the input node between $Rs1$ and C_{31} of Fig. 4,

TABLE 1. Design 1 results (including $L_{tune} = 12.42\,\mu$H).

Parameter	Design Goal	Simulation Result
Design H(z)	$\frac{-4623.02z^3-4069.63z^2-201.519z-30.7068}{z^3-0.31z^2+41.0114z+65.363}$	
T (nS)	25	N/A
τ (nS)	37.5	N/A
R_{adc}=R_{dac}=R_{io} (ohms)	30,000	N/A
f_1, f_2, f_3 (MHz)	$9.0, 10.0, 11.0$	N/A
$Z_{in}(s_1)$ (ohms)	$0.1 - 0.5j\left[Re\left(Z_{ant}(s_1)\right) - R_s + 0.1\right] - jIm\left(Z_{ant}(s_1)\right) - j2\pi f_1 L_{tune} \approx 0.1 + j176.4227$	N/A
$Z_{in}(s_2)$ (ohms)	$0.9 - jIm\left(Z_{ant}(s_2)\right) - j2\pi f_2 L_{tune} \approx 0.93 + j0.2591$	N/A
$Z_{in}(s_3)$ (ohms)	$0.1 + 0.5j\left[Re\left(Z_{ant}(s_3)\right) - R_s + 0.1\right] - jIm\left(Z_{ant}(s_3)\right) - j2\pi f_3 L_{tune} \approx 0.1 - j158.2057$	N/A
$Z_{tot}(s_1)$ (ohms)	$3.03 - j1.515$	$3.03 - j1.51$
$Z_{tot}(s_2)$ (ohms)	$4.56 + j0$	$4.57 + j0$
$Z_{tot}(s_3)$ (ohms)	$4.52 + j2.26$	$4.52 + j2.26$
Observed VSWR = 2 Bandwidth (MHz)		2.30
Theoretical Wheeler-Chu Bandwidth @ $ka = 0.42$ (MHz)		0.442
Observed Noise Figure (dB) @f_1, @f_2, @f_3		14.1, 12.7, 12.3
Maximum $G(z)$ System Pole Magnitude		0.9997

and e_{ant}^2 is the 290°K antenna radiation resistance noise referred back to the input node. The e_n noise voltages include the input-referred Johnson noise voltages of $0.13\sqrt{R}$ nV/$\sqrt{Hz}$ due to R_s, R_{adc}, R_{dac}, and R_{io}, plus an input-referred ADC noise voltage of 1 nV/$\sqrt{Hz}$ and an input-referred ADC noise due to a noise current of 2 pA/$\sqrt{Hz}$. The input-referred ADC noise voltage and noise current are based on an LTC6226 preamplifier for the ADC [44]. In computing noise figure as a radio receiver, R_s becomes the input impedance of the receiver, and the inclusion of the 290°K Johnson noise voltage of $0.13\sqrt{R_s}$ nV/$\sqrt{Hz}$ for R_s is equivalent to assuming a receiver noise figure of $10\log_{10}(1 + T_e/290) = 3$ dB [45].

In Table 1, the simulation results for the total tuned impedance $Z_{tot}(s)$ nearly equal the design goals at the three design frequencies. The plot of $Z_{tot}(s)$ and VSWR in Fig. 4 show that $Z_{tot}(s)$ closely equals the antenna radiation resistance near 10 MHz, with a reactance magnitude less than the radiation resistance. (Note that the real part of the passive-matched antenna impedance denoted $Re(Z_{pas})$ in Fig. 4 equals the antenna radiation resistance.) The simulation results in the solid curves of Fig. 4 closely match the theoretical results indicated by the ×'s in Fig. 4. Therefore, the proposed design method successfully achieves stable digital non-Foster impedance compensation for an ESA, with impedance bandwidth surpassing the Wheeler-Chu limit, and with simulation results that align well with theoretical predictions.

The second design example is the same as the first example in Fig. 3, except that the passive-tuning inductor is effectively removed by setting $L_{tune} = 0$. In this second example, the total impedance as seen by the voltage source is now $Z_{tot}(s) = Z_{ant}(s) + Z_{in}(s)$. As before, source resistance $Rs1 = 3.635$ corresponds to R_s in Fig. 1 and equals the antenna radiation resistance at frequency s_2. The antenna is again modeled by R_{31}, L_{31}, C_{31}, and C_{32}, but the passive-tuning inductor is effectively removed by setting $L_{tune} = 0$ in Fig. 1 and Fig. 3.

The digital filter $H(z)$ was again determined using the proposed design method, given the design goals for the second example given in Table 2 for the non-Foster impedance $Z_{in}(s)$ at the three design frequencies f_1, f_2, and f_3. The goals for $Z_{in}(s)$ approximately cancel the reactance of the antenna alone (since $L_{tune} = 0$), with a residual small resistance and a residual small reactance with positive slope. The corresponding $Z_{tot}(s) = Z_{in}(s) + Z_{ant}(s)$ are also given in Table 2 for the

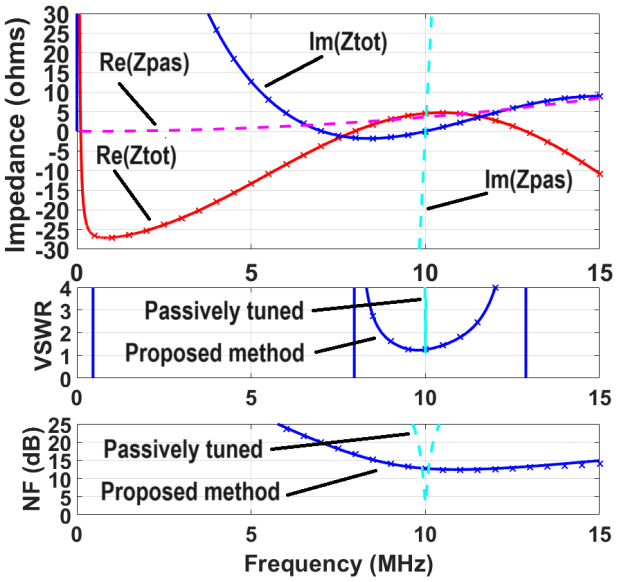

FIGURE 4. Simulation results for the design in Fig. 3 incorporating tuning inductor L_{tune}. (a) In the top plot, the solid curves show the real part $Re[Z_{tot}(s)]$ in red and imaginary part $Im[Z_{tot}(s)]$ in blue, where $Z_{tot}(s) = Z_{ant}(s) + sL_{tune}(s) + Z_{in}(s)$. Theoretical values for $Re[Z_{tot}(s)]$ and $Im[Z_{tot}(s)]$ are shown by $\times$'s. The real and imaginary parts of the passively-tuned antenna using L_{tune} alone are shown in dashed magenta for $Re(Z_{pas})$ and dashed cyan for $Im(Z_{pas})$, also noting that $Re(Z_{pas})$ equals the antenna radiation resistance. (b) In the middle plot, the solid blue curve shows simulated VSWR corresponding to $Z_{tot}(s)$, with theoretical VSWR shown by $\times$'s, and where VSWR=1 corresponds to an impedance equal to R_s of Fig. 1. The VSWR bandwidth of the passive-tuned antenna in the dashed cyan curve is too narrow to be resolved here. (c) In the bottom plot, the solid blue curve shows simulated noise figure assuming R_s of Fig. 1 in receiver mode is a 3 dB noise figure receiver, with theoretical values shown by $\times$'s. The dashed cyan curve shows the theoretical noise figure of the passively-tuned antenna.

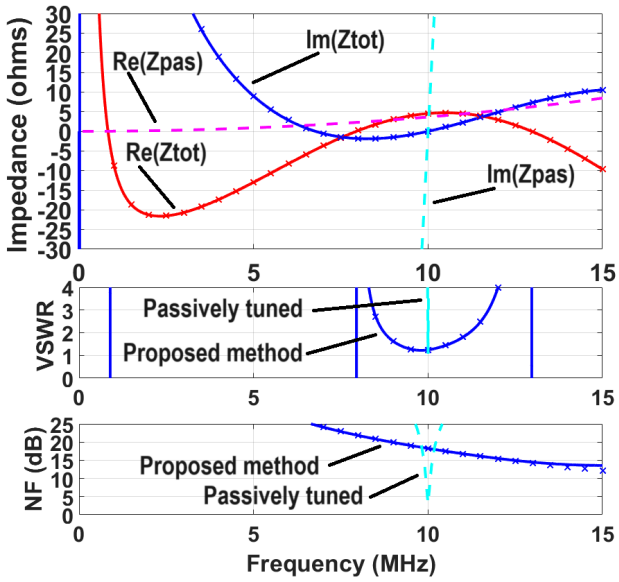

FIGURE 5. Simulation results for the design in Fig. 3, effectively removing the tuning inductor, by setting $L_{tune} = 0$. (a) In the top plot, the solid curves show the real part $Re[Z_{tot}(s)]$ in red and imaginary part $Im[Z_{tot}(s)]$ in blue, where $Z_{tot}(s) = Z_{ant}(s) + Z_{in}(s)$. Theoretical values for $Re[Z_{tot}(s)]$ and $Im[Z_{tot}(s)]$ are shown by $\times$'s. The real and imaginary parts of the 12.42 µH passively-tuned antenna are shown in dashed magenta for $Re(Z_{pas})$ and dashed cyan for $Im(Z_{pas})$, also noting that $Re(Z_{pas})$ equals the antenna radiation resistance. (b) In the middle plot, the solid blue curve shows simulated VSWR corresponding to $Z_{tot}(s)$, with theoretical VSWR shown by $\times$'s, and where VSWR = 1 corresponds to an impedance equal to R_s of Fig. 1. The VSWR bandwidth of the passive-tuned antenna in the dashed cyan curve is too narrow to be resolved here. (c) In the bottom plot, the solid blue curve shows simulated noise figure assuming R_s of Fig. 1 in receiver mode is a 3 dB noise figure receiver, with theoretical values shown by $\times$'s. The dashed cyan curve shows the theoretical noise figure of the passively-tuned antenna.

three design frequencies. For this second example, the new digital filter design $H(z)$ is provided in Table 2 using our proposed design method, and is incorporated in $H(z)$ of Fig. 3.

In the top plot of Fig. 5, simulation results for $Z_{tot}(s) = Z_{ant}(s) + Z_{in}(s)$ are plotted as the solid curves, along with $\times$'s showing the theoretical $Z_{tot}(s)$. The solid red curve shows the real part $Re[Z_{tot}(s)]$, and the solid blue curve shows the imaginary part $Im[Z_{tot}(s)]$. The real and imaginary parts of a 12.42 µH passively-tuned antenna are shown in the dashed magenta and dashed cyan curves, respectively. Both the real and imaginary parts of the simulated $Z_{tot}(s)$ closely match the theoretical $Z_{tot}(s)$ in the top plot of Fig. 5.

As shown in the middle plot of Fig. 5, the VSWR = 2 bandwidth of the simulation was 2.3 MHz centered around 9.9 MHz. The Wheeler-Chu bandwidth-efficiency product from (21) for a center frequency of 10 MHz with $ka = 0.42$ rad is $B\eta = 0.0442$ or approximately 440 kHz. This second example demonstrates the design's effectiveness in increasing the bandwidth to approximately $2.3/0.442 = 5.2$ times the Wheeler-Chu limit for $\eta = 1$ (or 4.2 if we let $\eta \approx 3.63/4.54 = 0.8$ due to the added $0.9\,\Omega$ in $Z_{in}(s_2)$ at f_2 as noted in Table 2). The 2.3 MHz bandwidth is again 48.9 times the theoretical passive-tuned antenna bandwidth.

The simulated noise figure is shown as the solid blue curve in the bottom plot of Fig. 5, with $\times$'s showing the theoretical noise figure. The dashed cyan curve shows the theoretical noise figure of a 12.42 µH passively-tuned antenna. The noise figure is also noted in Table 2 at design frequencies f_1, f_2, and f_3. The noise figure NF is calculated from the simulation in the same manner as the first example. At the mid-band frequency f_2, this second example's noise figure is approximately 5.5 dB worse than in the first example.

As seen in Table 2, the simulation results for the total tuned impedance $Z_{tot}(s)$ nearly equal the design goals at the three design frequencies. The plots of $Z_{tot}(s)$ and VSWR in Fig. 5 show that $Z_{tot}(s)$ closely equals the antenna radiation resistance denoted as $Re(Z_{pas})$ near 10 MHz, with a reactance magnitude less than the radiation resistance. The simulation results in the solid curves of Fig. 5 closely match the theoretical results shown by the $\times$'s in Fig. 5. Thus, the proposed design method

TABLE 2. Design 2 results (without L_{tune}).

Parameter	Design Goal	Simulation Result
Design H(z)	$\frac{4889.27z^3-4610.91z^2+50.0224z-13.856}{z^3-0.49z^2+53.4003z+51.4956}$	
f_1, f_2, f_3 (MHz)	9.0, 10.0, 11.0	N/A
T (nS)	25	N/A
τ (nS)	37.5	N/A
$R_{adc} = R_{dac} = R_{io}$ (ohms)	30,000	N/A
$Z_{in}(s_1)$ (ohms)	$0.1 - 0.5j\left[Re\left(Z_{ant}(s_1)\right) - R_s + 0.1\right] - jIm\left(Z_{ant}(s_1)\right) \approx 0.1 + j878.7571$	N/A
$Z_{in}(s_2)$ (ohms)	$0.9 - jIm\left(Z_{ant}(s_2)\right) \approx 0.9 + j780.6307$	N/A
$Z_{in}(s_3)$ (ohms)	$0.1 + 0.5j\left[Re\left(Z_{ant}(s_3)\right) - R_s + 0.1\right] - jIm\left(Z_{ant}(s_3)\right) \approx 0.1 + j700.2031$	N/A
$Z_{tot}(s_1)$ (ohms)	$3.03 - j1.515$	$3.03 - j1.51$
$Z_{tot}(s_2)$ (ohms)	$4.53 + j0$	$4.54 + j0$
$Z_{tot}(s_3)$ (ohms)	$4.52 + j2.26$	$4.52 + j2.26$
Observed VSWR = 2 Bandwidth (MHz)		2.3
Theoretical Wheeler-Chu Bandwidth @ $ka = 0.42$ (MHz)		0.442
Observed Noise Figure (dB) @f_1, @f_2, @f_3		19.9, 18.2, 16.7
Maximum $G(z)$ System Pole Magnitude		0.9831

TABLE 3. Comparison with Prior Non-Foster Results

Reference	Chu Limit Parameter ka	Theoretical Chu Limit Fractional Bandwidth	Observed Fractional Bandwidth	Ratio of Observed to Theoretical
Fig. 4	0.44	0.044	0.23	5.2
Fig. 5	0.44	0.044	0.23	5.2
Ref. [11]	0.39	0.036	0.039	1.1
Ref. [14]	0.27	0.020	1.65	49.7

has again provided stable digital non-Foster impedance compensation of an ESA with bandwidth exceeding the Wheeler-Chu limit, where the simulation results closely match theory.

Since every simulation was conducted in the time domain with causal RLC components and causal $H(z)$, frequency-domain results in Fig. 4 and Fig. 5 must satisfy the Kramers-Kronig relations. Furthermore, the frequency-domain simulation results in Fig. 4 and Fig. 5 are created from the Fourier transform of the stable and causal time-domain simulation of the system.

It is somewhat difficult to compare non-Foster ESA design results, because the design and geometry of underlying antenna strongly impacts achieved bandwidth and is often limited by application constraints. Nevertheless, Table 3 compares the re-

sults of Fig. 4 and Fig. 5 to results in [11] and [14]. The second column of the table gives the Wheeler-Chu parameter ka, and the third column gives the theoretical Wheeler-Chu bandwidth limit B, assuming efficiency $\eta = 1$ and with requisite adjustments to (21) for VSWR from [3]. The third column of the table gives the observed fractional bandwidth, and the fourth column gives the improvement ratio of the observed fractional bandwidth to theoretical fractional bandwidth. The improvement ratio of our proposed method exceeds the results in [11]. The much greater improvement ratio of [14] may be attributed to the use of a lower-Q large-volume cylindrical slot antenna instead of a dipole.

5. CONCLUSION

A method for the design of a stable digital non-Foster impedance match to an electrically small antenna has been presented. Example designs demonstrated stable digital non-Foster impedance matching to an electrically small dipole. The examples achieved VSWR = 2 bandwidths between 4.15 and 5.2 times the theoretical Wheeler-Chu bandwidth for an electrically small dipole antenna having Q = 215 and ka = 0.42 rad. The bandwidth is also 48.9 times the theoretical passive-tuned antenna bandwidth. While the results show that our method can create designs that exceed the Wheeler-Chu impedance bandwidth, improvements might be achieved by:

- altering the heuristic choice of design impedance goals,
- using more than three frequencies to solve for digital filter coefficients,
- increasing the order of H(z),
- increasing the number of free variables allowed in H(z),
- using reactive feedback in place of R_{io}.

Significantly, both theory and simulation confirm that digital non-Foster circuits can provide impedance matching bandwidth greater than the Wheeler-Chu limit for electrically small antennas.

DATASET

A dataset for all examples is at [43], with encryption password aa4488gg.

ACKNOWLEDGEMENT

This material is based upon work supported by the National Science Foundation under Grant No. 1731675.

REFERENCES

[1] Chu, L. J., "Physical limitations of omnidirectional antennas," *Journal of Applied Physics*, Vol. 19, No. 12, 1163–1175, 1948.

[2] Wheeler, H. A., "Fundamental limitations of small antennas," *Proceedings of the IRE*, Vol. 35, No. 12, 1479–1484, Dec. 1947.

[3] Sievenpiper, D. F., D. C. Dawson, M. M. Jacob, T. Kanar, S. Kim, J. Long, and R. G. Quarfoth, "Experimental validation of performance limits and design guidelines for small antennas," *IEEE Transactions on Antennas and Propagation*, Vol. 60, No. 1, 8–19, Jan. 2012.

[4] Dagefu, F. T., J. Choi, B. M. Sadler, and K. Sarabandi, "A survey of small, low-frequency antennas: Recent designs, practical challenges, and research directions," *IEEE Antennas and Propagation Magazine*, Vol. 65, No. 1, 14–26, 2021.

[5] Linvill, J. G., "Transistor negative-impedance converters," *Proceedings of the IRE*, Vol. 41, No. 6, 725–729, Jun. 1953.

[6] Sedra, A., G. W. Roberts, and F. Gohh, "The current conveyor: History, progress and new results," in *Circuits, Devices and Systems, IEE Proc. G*, Vol. 137, No. 2, 78–87, 1990.

[7] Sussman-Fort, S. E. and R. M. Rudish, "Non-Foster impedance matching of electrically-small antennas," *IEEE Transactions on Antennas and Propagation*, Vol. 57, No. 8, 2230–2241, Aug. 2009.

[8] Barbuto, M., A. Monti, F. Bilotti, and A. Toscano, "Design of a non-Foster actively loaded SRR and application in metamaterial-inspired components," *IEEE Transactions on Antennas and Propagation*, Vol. 61, No. 3, 1219–1227, Mar. 2013.

[9] Buiantuev, B., N. Kalmykov, D. Kholodnyak, A. Brizić, L. Vincelj, and S. Hrabar, "Physically oriented design of negative capacitors based on Linvill's floating impedance converter," *IEEE Transactions on Microwave Theory and Techniques*, Vol. 70, No. 1, 139–154, 2022.

[10] Gregoire, D. J., C. R. White, and J. S. Colburn, "Wideband artificial magnetic conductors loaded with non-foster negative inductors," *IEEE Antennas and Wireless Propagation Letters*, Vol. 10, 1586–1589, 2011.

[11] Shi, T., M.-C. Tang, Z. Wu, H.-X. Xu, and R. W. Ziolkowski, "Improved signal-to-noise ratio, bandwidth-enhanced electrically small antenna augmented with internal non-foster elements," *IEEE Transactions on Antennas and Propagation*, Vol. 67, No. 4, 2763–2768, 2019.

[12] Shih, T.-Y. and N. Behdad, "Wideband, non-Foster impedance matching of electrically small transmitting antennas," *IEEE Transactions on Antennas and Propagation*, Vol. 66, No. 11, 5687–5697, 2018.

[13] Choi, J., F. T. Dagefu, B. M. Sadler, and K. Sarabandi, "A miniature actively matched antenna for power-efficient and bandwidth-enhanced operation at low VHF," *IEEE Transactions on Antennas and Propagation*, Vol. 69, No. 1, 556–561, 2021.

[14] Jacob, M. M. and D. F. Sievenpiper, "Non-Foster matched antennas for high-power applications," *IEEE Transactions on Antennas and Propagation*, Vol. 65, No. 9, 4461–4469, Sep. 2017.

[15] Vincelj, L., R. W. Ziolkowski, and S. Hrabar, "Experimental demonstration of non-Foster self-oscillating Huygens radiator," in *2020 Fourteenth International Congress on Artificial Materials for Novel Wave Phenomena (Metamaterials)*, 508–510, New York, NY, USA, Sep. 2020.

[16] White, C. R., J. S. Colburn, and R. G. Nagele, "A non-Foster VHF monopole antenna," *IEEE Antennas and Wireless Propagation Letters*, Vol. 11, 584–587, 2012.

[17] Mirzaei, H. and G. V. Eleftheriades, "A resonant printed monopole antenna with an embedded non-foster matching network," *IEEE Transactions on Antennas and Propagation*, Vol. 61, No. 11, 5363–5371, Nov. 2013.

[18] Rasmussen, C. and A. Alù, "Non-Foster acoustic radiation from an active piezoelectric transducer," *Proceedings of the National Academy of Sciences*, Vol. 118, No. 30, e2024984118, 2021.

[19] Hayran, Z. and F. Monticone, "Using time-varying systems to challenge fundamental limitations in electromagnetics: Overview and summary of applications," *IEEE Antennas and Propagation Magazine*, Vol. 65, No. 4, 29–38, 2023.

[20] Mekawy, A., H. Li, Y. Radi, and A. Alù, "Parametric enhancement of radiation from electrically small antennas," *Physical Re-*

view Applied, Vol. 15, No. 5, 054063, May 2021.

[21] Loghmannia, P. and M. Manteghi, "Broadband parametric impedance matching for small antennas using the Bode-Fano limit: Improving on Chu's limit for loaded small antennas," *IEEE Antennas and Propagation Magazine*, Vol. 64, No. 5, 55–68, 2022.

[22] Fano, R. M., "Theoretical limitations on the broadband matching of arbitrary impedances," *Journal of the Franklin Institute*, Vol. 249, No. 1, 57–83, 1950.

[23] Bode, H., *Network Analysis and Feedback Amplifier Design, ser.*, The Bell Telephone Laboratories Series. Van Nostrand, 1945.

[24] Carlin, H. and P. Crepeau, "Theoretical limitations on the broadband matching of arbitrary impedances," *IRE Transactions on Circuit Theory*, Vol. 8, No. 2, 165–165, 1961.

[25] Ugarte-Munoz, E., S. Hrabar, D. Segovia-Vargas, and A. Kiricenko, "Stability of non-Foster reactive elements for use in active metamaterials and antennas," *IEEE Transactions on Antennas and Propagation*, Vol. 60, No. 7, 3490–3494, Jul. 2012.

[26] Stearns, S. D., "Incorrect stability criteria for non-Foster circuits," in *Proceedings of the 2012 IEEE International Symposium on Antennas and Propagation*, 1–2, Chicago, IL, USA, Jul. 2012.

[27] Stearns, S. D., "Stable band-pass non-Foster circuits," in *2015 IEEE International Symposium on Antennas and Propagation & USNC/URSI National Radio Science Meeting*, 1386–1387, Vancouver, BC, Canada, Jul. 2015.

[28] Ugarte-Muñoz, E., S. Hrabar, and D. Segovia-Vargas, "Investigation of stability of negative impedances for use in active metamaterials and antennas," in *Proceedings of the 5th European Conference on Antennas and Propagation (EUCAP)*, 2059–2063, Rome, Italy, Apr. 2011.

[29] Xu, Z., M. W. Yung, D. A. Hitko, and C. R. White, "Non-foster circuit stabilization method," US Patent 9,054,798, Jun. 2015.

[30] Daniel, C. G. and T. P. Weldon, "A stable digital impedance circuit design method for resistive source impedances," *IEEE Open Journal of Circuits and Systems*, Vol. 3, 109–114, 2022.

[31] Weldon, T. P., "Digital discrete-time non-foster circuits and elements," US Patent 10,073,812, Sep. 2018.

[32] Kehoe, P. J., K. K. Steer, and T. P. Weldon, "Thevenin forms of digital discrete-time non-Foster RC and RL circuits," in *2016 IEEE International Symposium on Antennas and Propagation (APSURSI)*, 191–192, Fajardo, PR, USA, Jun. 2016.

[33] Weldon, T. P., J. M. C. Covington, K. L. Smith, and R. S. Adams, "Stability conditions for a digital discrete-time non-Foster circuit element," in *2015 IEEE International Symposium on Antennas and Propagation & USNC/URSI National Radio Science Meeting*, 71–72, Vancouver, BC, Canada, Jul. 2015.

[34] Friis, H. T., "A note on a simple transmission formula," *Proceedings of the IRE*, Vol. 34, No. 5, 254–256, May 1946.

[35] Weldon, T. P., "Use of a digital non-foster radio architecture for conventional tuning of electrically-small antennas," in *2018 IEEE International Symposium on Antennas and Propagation & USNC/URSI National Radio Science Meeting*, 1921–1922, Boston, MA, USA, Jul. 2018.

[36] Weldon, T. P., "A digital non-foster VHF radio approach for enabling low-power internet of things," in *2020 IEEE International Symposium on Circuits and Systems (ISCAS)*, 1–5, Seville, Spain, Oct. 2020.

[37] Smith, K. L., R. S. Adams, and T. P. Weldon, "Measurement of a fast-wave line using digital non-foster circuits for software-adjustable delay," in *2016 IEEE International Symposium on Antennas and Propagation (APSURSI)*, 193–194, Fajardo, PR, USA, Jun. 2016.

[38] Hecht, K. A., C. G. Daniel, and T. P. Weldon, "Effect of external source impedance on the input impedance of digital impedance circuits," in *2020 IEEE International Symposium on Circuits and Systems (ISCAS)*, 1–5, Seville, Spain, Oct. 2020.

[39] Phillips, C. and H. Nagle, *Digital Control System Analysis and Design*, Prentice-Hall, 1990.

[40] Oppenheim, A. V. and R. W. Schafer, *Discrete-time Signal Processing*, 3rd ed., Prentice Hall, 2009.

[41] Tang, T. G., Q. M. Tieng, and M. W. Gunn, "Equivalent circuit of a dipole antenna using frequency-independent lumped elements," *IEEE Transactions on Antennas and Propagation*, Vol. 41, No. 1, 100–103, Jan. 1993.

[42] Temes, G. C. and J. W. LaPatra, *Introduction to Circuit Synthesis and Design*, McGraw Hill Book Company, 1977.

[43] Weldon, T., "(PASSWORD aa4488gg) Rev. 1 dataset for digital non-foster impedance design for wideband electrically small antennas beyond the Chu limit," [Online]. Available: https://dx.doi.org/10.21227/681s-w872, 2024.

[44] Analog Devices, Inc., "LTC6226-6227: 1nV/√ Hz 420 MHz GBW, 180 V/µs, low distortion rail-to-rail out-put op amps data sheet (Rev.0)," [Online]. Available: https://www.analog.com/media/en/technical-documentation/data-sheets/ltc6226-6227.pdf.

[45] Pozar, D. M., *Microwave Engineering*, 3rd ed., Wiley, Hoboken, NJ, 2005.